Journal of The Electrochemical Society, **161** (8) E3001-E3008 (2014)
0013-4651/2014/161(8)/E3001/8/$31.00 © The Electrochemical Society

JES Focus Issue on Mathematical Modeling of Electrochemical Systems at Multiple Scales

Numerical Scaling Studies of Kinetically-Limited Electrochemical Nucleation and Growth with Accelerated Stochastic Simulations

Andri Bezzola,[a,*,z] Benjamin B. Bales,[a,z] Linda R. Petzold,[b] and Richard C. Alkire[c,]**

[a]*Mechanical Engineering Department, University of California, Santa Barbara, California 93106, USA*
[b]*Mechanical Engineering Department and Computer Science Department, University of California, Santa Barbara, California 93106, USA*
[c]*Department of Chemical and Biomolecular Engineering, University of Illinois, Urbana, Illinois 61801, USA*

A stochastic atomic-scale lattice-based numerical method based on the Exact Lattice First Passage Time method was developed for the simulation of the early stages of kinetically controlled electrochemical nucleation and growth. Electrochemical reaction and surface diffusion on a hexagonal lattice was accounted for in a pristine physical model system that included edge diffusion along steps, and movement over step edges with Ehrlich-Schwöbel barrier. Five cases were investigated: homoexpitaxy, heteroepitaxy, multi-layer growth, terraces, and confined regions. For each, the influence of the physical parameters, deposition conditions, and system geometry on growth morphology was investigated. Simulation based studies of multilayer surface morphology were able to distinguish between layer-by-layer and island growth modes. On stepped terraces, parameter regions associated with he surface diffusion to deposition flux ratio (D/F) and the Ehrlich-Schwöbel barrier were identified under which deposition occurred either at the step edge or by nucleation and growth of islands on the terraces. The probability of growing single crystals in a small confined region was found to scale with D/F and the radius squared.
© 2014 The Electrochemical Society. [DOI: 10.1149/2.001408jes] All rights reserved.

Manuscript received December 27, 2013. Published February 25, 2014. *This paper is part of the JES Focus Issue on Mathematical Modeling of Electrochemical Systems at Multiple Scales.*

Precise control of the early stages of nucleation and growth during electrochemical deposition is important for many practical devices for which fabrication and/or functional operation depends critically on deposit structure at the nanoscale. Examples of atomic-scale tuning of surface structures to achieve electrical, magnetic, optical, or other properties may be found in semiconductor and mass-storage devices, solar cells, and batteries[1–5] as well as numerous conceptual systems currently in laboratory or early-development stages.[6–12] These activities are driving development of improved numerical approaches for investigating how deposition features depend upon movement of incoming atoms by reaction, surface diffusion and attachment to growth sites.

While there is a large literature on theory and modeling of electrodeposition at the continuum scale,[13–15] the use of kinetic Monte Carlo (KMC) and other molecular simulation methods[16] has proven useful in the study of small-scale reaction/diffusion phenomena during electrodeposition. However, the KMC method can be time-consuming under conditions encountered when surface adatoms diffuse rapidly over large distances before taking part in nucleation or lattice growth events. In this work, we report on extending the Exact Lattice First Passage Time (ELFPT) approach[17] to encompass a wider range of physical processes while maintaining the accuracy and efficiency of simulations of atomic-scale on-lattice electrodeposition events. The method is used to investigate five categories of model systems, and to explore regions of parameter space where the efficiency of classic KMC methods is challenged. Numerical results are reported that characterize the growth modes and scaling parameters that govern the behavior of these systems.

The following choice of five categories of model systems for investigation was inspired by their widespread use in previous experimental and theoretical studies as reported below: (1) Homoepitaxial nucleation and growth; (2) Heteroepitaxial nucleation and growth; (3) Multi-layer growth on flat surfaces; (4) Growth on terraced surfaces; and (5) Nucleation and growth of single crystals in a confined region. It is abundantly clear, however, that realistic electrodeposition systems involve many phenomena in addition to those considered in this work. Our goal is to provide an initial step in bridging between simulation and experiment with tractable model systems.

*Electrochemical Society Student Member.
**Electrochemical Society Fellow.
zE-mail: andri.bezzola@gmail.com; bbbales2@gmail.com

Although surface diffusion phenomena are central to all of the foregoing experimental investigations, there is a paucity of measured data for surface diffusion coefficients. The existing data and methods of estimating values for surface diffusion coefficients have been reviewed[18,19] for a wide variety of systems that include metals, semiconductors and insulators. Of these, experimental data for surface diffusivities under liquid solution are reported for only a few systems involving pure metal (Au on Au and Pt on Pt). For a small number of additional systems, the surface diffusivities and energy barriers were estimated by a combination of simulation and experiments.

A review is available[16] of recent developments in electrochemical applications involving multi scale molecular simulation. Many nucleation and growth applications have been numerically simulated with some variant of KMC methods,[20] adding phenomena like diffusion along step edges,[21] Ehrlich-Schwöbel barriers,[22] among others. However, the KMC technique can be demanding on computational resources. Such circumstances can render certain simulations impractical or even impossible[23] and severely limit the parameter space for test cases,[24] especially when the disparity between time- and length-scales in the process is large. Coarse-grained KMC methods[25,26] as well as hybrid continuum-KMC methods,[27–29] and Island Dynamics methods,[30–32] have been developed for use in simulation of electrodeposition processes.[33–36] These, however, do not provide accuracy at the atomic scale where nucleation occurs.[37]

Important theoretical contributions to surface-diffusion-controlled nucleation have been made based on point-island calculations.[38,39] The influence of surface diffusion on shape of nanocrystals,[40] nearest-neighbor relationships,[41] and shape evolution[28] has been reported. The influence of overpotential on island growth in homoepitaxial and heteroepitaxial systems[42,43] has been reported along with analytical formulas to be used in conjunction with experimental results to extrapolate physical parameters from measured data.

Krug et al. present a theory for the calculation of island nucleation on terraces in the case of multi-layer growth[44] and note that, while their theory is best suited for situations with large Ehrlich-Schwöbel barriers, it would be desirable to develop methods to predict multilayer growth with intermediate and weak barriers.

In the next section, we briefly summarize the ELFPT method. We then introduce important new capabilities that were required for simulation of the model systems. Finally, we will discuss results obtained with the simulations and provide conclusions on growth modes and empirical scaling parameters.

Downloaded on 2014-06-20 to IP 128.111.41.122 address. Redistribution subject to ECS terms of use (see ecsdl.org/site/terms_use) unless CC License in place (see abstract).

Computational Methodology

Exact lattice first passage time (ELFPT) approach.— The ELFPT method is based on the First Passage Time (FPT) approach,[45–48] which we have modified for systems where epitaxial electrodeposition onto lattices takes place. FPT replaces the atomic scale diffusive motion of surface adatoms in KMC by larger hops based on solutions to the diffusion equation.[49,50]

The algorithm for FPT and ELFPT algorithms contains the following steps: (1) Adatoms can appear on the deposit surface at influx rate F. The arrival time of the next adatom is stored in an event queue and the arrival location is chosen randomly over the possible sites. (2) Adatoms move around the surface by random walks which consist of hops to directly neighboring sites. The hopping rate is calculated from the surface diffusivity constant D. Each diffusing adatom is assigned a protection zone. The protection zones are adaptively constructed in such a way that they each contain only one adatom and do not overlap any existing deposit sites. This allows for the use of solutions to the diffusion equation for calculation of exit times, because the adatoms perform unrestricted random walks within the protection zone. The random walks are not explicitly tracked within the protection zones. Instead, a first passage time is calculated when the adatoms first exit their protection zone. Exit times for all adatoms are stored in the event queue. (3) The event with the next lowest time in the event queue is executed and protection zones are updated as needed. (4) For protection zones that need updating, a no-passage (NP)[46] propagator is employed to ensure that the location of the adatom is accurate for the current time. Atomic scale accuracy is given by the flexibility of the protection zones to shrink to a single site in neighborhood of other adatoms or step edges. At this point the algorithm reverts to standard KMC. Thus there is no need to decide a priori whether to use ELFPT or KMC; the ELFPT algorithm shifts to KMC as necessary.

The ELFPT method takes advantage of the fact that adatoms move around on surfaces that have a physical lattice structure. It restricts the diffusive motion of adatoms to discrete random walks on lattice structures. While the calculation of first passage times in continua requires the numerical calculation of the Green's function, the first passage time on discrete lattices can be calculated efficiently in closed form.[17]

The ELFPT method is accurate over large distances with atomic scale resolution, and is considerably faster for conditions where the (D/F) ratio is high. The performance of ELFPT relies on the ability to quickly compute exact exit-time distributions and to determine distances to the nearest walker and deposited islands. For ideal situations where adatoms diffuse over large distances before nucleating or attaching to islands, it was found[17] that the method achieved a speedup up to 100× over comparable KMC simulations.

Physical model of electrodeposition.— Our goal is to provide an initial step toward bridging between simulations and experiments in simple systems. Realistic electrodeposition systems involve many phenomena, of which those considered here represent only a small but important subset. We assumed that electrodeposition reactions generate a flux density (F) of adatoms on the surface (hcp(0002)), which then diffuse around the surface by random walks with diffusivity coefficient D. Adatoms that move into adjacent positions form a nucleus (defined here to be two adjacent adatoms), that were assumed to remain immobile thereafter. Additional adatoms that collide with the nucleus were assumed to attach to it irreversibly, and were allowed to diffuse along the edge before depositing.

The crystal structure of the substrate was chosen to be hexagonal, corresponding to fcc(111) or hcp(0002). Unlike the (100) surface structure investigated previously,[17] for which the FPT distribution was calculated analytically, the fcc(111) and hcp(0002) structures have three non-independent directions for a diffusive hop, rendering the solution of the diffusion equation non-separable. Instead, the FPT distributions were pre-calculated by computing the matrix exponential as the solution to the discrete Laplacian operator and stored in a lookup table. For the hexagonal lattice surface, simulations were restricted to the ABAB stacking sequence found in crystals with hcp unit lattices. The method extends in a straightforward manner to the ABCABC stacking order of crystals with an fcc unit lattice.

Edge diffusion of adatoms along island boundaries can represent a major KMC computation cost;[51] the FPT approach was therefore used in a manner analogous to the lookup table approach described in the previous paragraph. To allow for larger edge diffusion hops, we included hops around corners. For simplicity, it was assumed that the edge diffusion coefficient was proportional to the surface diffusivity

$$D_{edge} = \beta D. \qquad [1]$$

Comparison of experimental results[52] and simulations[53] suggests that edge diffusion can be orders of magnitude faster than surface diffusion.

Heteroepitaxial growth was simulated by implementing two deposition fluxes, one onto the substrate (F_S), and another onto the previously deposited metal (F_M). No account was taken of lattice mismatch between the two materials. Multi-layer growth was accommodated by permitting adatoms to nucleate and grow on top of previously deposited islands. Movement of adatoms over an edge onto lower layers was assumed to obey an Ehrlich-Schwöbel (ES) barrier, and was simulated via a hopping rate D_{ES} that was assumed to be proportional to the rate of surface diffusion:

$$D_{ES} = \gamma D, \qquad [2]$$

Software.— The software was written in C++ and parallelized over the different parameters and the number of ensemble runs in each executed parameter sweep. The code can be run on a single core of a desktop computer or laptop. Parallelization of ensembles of runs is trivial and can be achieved in any environment with multiple processors. We have used a Hadoop-cluster of personal desktop computers to evaluate the parameter-sweeps for the results presented in this paper. We note that for large systems, the memory size of the FPT lookup table can reach the gigabyte range. The size of the lookup-table scales with the size of the largest possible protection zone.

Results

Table I lists the five model systems that were investigated, along with the ranges for the parameters (D/F), β , and γ for which numerical results were obtained. The following sections summarize each system.

Homoepitaxy.— Fundamental experimental studies on electrodeposition have been carried out by a various methods that include surface imaging.[7,8,54–59] These investigations provide unparalleled insight into single crystal homoepitaxial growth at the solid-liquid interface, which can deviate significantly from features observed in systems operated under ultra-high vacuum.[60]

The homoepitaxial system was used to validate the results in this paper against previously published surface nucleation and growth calculations. Simulations were carried out for sub-monolayer coverage by electrodeposition onto an atomically flat initial surface (HCP(0002)) for various values of (D/F). The simulation domain size was chosen to be 256×256 with periodic boundary conditions in all directions, which was found to result in at least 20 nuclei at final coverage of $\theta = 0.5$, even for the highest (D/F) values. Results were

Table I. Cases investigated.

Case	D/F range	β	γ
Homoepitaxy	10^3 to 10^9	10^{-6} to 10^{-2}	1
Heteroepitaxy	10^3 to 10^{10}	10^{-2}	1
Multilayer Growth	10^3 to 10^9	10^{-2}	10^{-5} to 1
Growth on Stepped Terraces	10^3 to 10^9	10^{-3} to 1	10^{-3} to 10^3
Single Crystal in confined area	10^4 to 10^{10}	10^{-2}	1

Downloaded on 2014-06-20 to IP 128.111.41.122 address. Redistribution subject to ECS terms of use (see ecsdl.org/site/terms_use) unless CC License in place (see abstract).

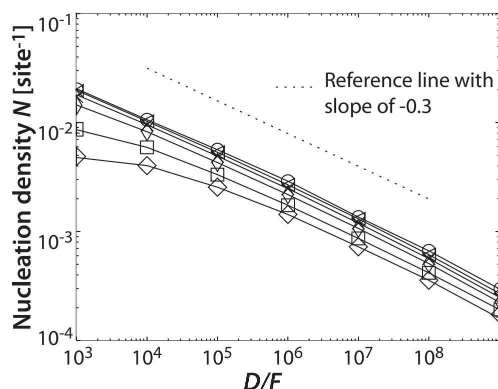

Figure 1. Homoepitaxy, $\beta = 0.01$, $\gamma = 1$. Dependence of average nucleation density N with the ratio of (D/F). Results are shown for coverages of $\theta = 0.01$ ML (◇), $\theta = 0.02$ ML (□), $\theta = 0.05$ ML (◊), $\theta = 0.1$ ML (×), $\theta = 0.2$ ML (△), and $\theta = 0.5$ ML (◯). A dotted line with slope of -0.3 is plotted for reference.

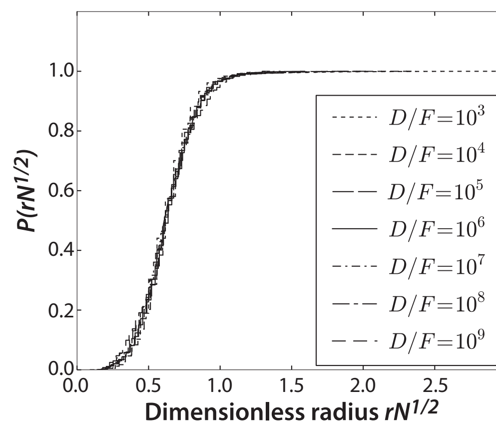

Figure 2. Scaling of probability to find the COM of at least one neighbor within the scaled radius $rN^{1/2}$. Results are plotted at a coverage of $\theta = 0.5$ for values of (D/F) ranging from 10^3 to 10^9.

numerically analyzed in order to report on nucleation density, and the distribution of nearest-neighbor distances.

Figure 1 shows computed results for the dependence of nucleation density (N) on the ratio (D/F) for values of surface coverage between $0.01 < \theta < 0.5$ equivalent monolayers (ML) for $\beta = 0.01$ and $\gamma = 1$. Each data point in Figure 1 represents the average value of 50 simulation runs with identical parameters. It should be noted that for homoepitaxial systems, it does not matter for these simulations whether D or F is varied, but for completeness we report that we kept D constant $(D = 1)$ and varied the value of F $(F = 10^-3$ to $10^-9)$.

It has been shown previously[38] that the nucleation density N, of point islands follows the relation

$$N \propto (D/F)^{-\chi} \quad [3]$$

for a fixed amount of sub-monolayer coverage. In that paper the authors reported a value $\chi = 0.3$ for simulations with point nuclei and isotropic diffusion, while the mean field rate equations predicted a factor of $\chi = 1/3$ as $(D/F) \to \infty$.

These values compare favorably with our simulations of islands with finite sizes, shown in Figure 1. When plotting N versus (D/F) in a log-log plot, the slope of the lines corresponds to the value of $-\chi$. We have plotted results for various values of (D/F) and θ and have included a dotted reference line with slope -0.3. Values between $\chi = 0.302$ to $\chi = 0.309$ were obtained for conditions of coverage $\theta > 0.05$ ML and all values of $(D/F) > 10^6$. For the range of parameters under investigation here, it was only for $(D/F) < 10^4$, that the nucleation density changed considerably (more than $5\times$) from $\theta = 0.01$ ML to $\theta = 0.5$ ML. For all other values of (D/F), the nucleation density changed less than a factor of $3\times$ between coverages of $\theta = 0.01$ and $\theta = 0.5$, indicating instantaneous nucleation.

For islands of finite size investigated here, we define the nearest-neighbor distance d_{NN} as the minimal distance from the center of mass (COM) of one island to the COMs of its neighboring islands, and denote the probability distribution for finding the COM of at least one neighbor at distance r from the COM of any given island by $P(r)$. Figure 2 shows the probability distribution, $P(rN^{1/2})$, of finding at least one nearest-neighbor within the scaled radius $(rN^{1/2})$ for a range of (D/F) values at $\theta = 0.5$. The observation that all the curves lie on top of each other supports the observation that the nearest-neighbor distance distribution scales with $N^{1/2}$, even for islands of finite size at relatively high coverage. These homoepitaxy results are in agreement with the findings for point-size islands[38] and serve as an empirical validation of the code developed in the present study.

For the case of pure homoepitaxy, it is not unusual to obtain a speedup of ELFPT over KMC of $20\times$ or $30\times$, as reported previously.[17] Highest speedups are reported for high values of (D/F) and low values of β. The speedup of the ELFPT algorithm is limited by length of kink-free edge segments. Larger values of β result in more compact island shapes and larger straight edges, where the FPT approach for edge diffusion is most beneficial. The performance gain of ELFPT over KMC in simulations with high β is limited. This is a result from the larger relative computation time spent on edge-diffusion events compared with surface diffusion events in simulations with large β. 1-D edge diffusion FPT does not provide the same amount of speedup as 2-D surface diffusion FPT.

Heteroepitaxy.— Experimental investigation of multilayer electrodeposition of up to four monolayers of Pd on Au(100) were carried out by X-ray diffraction and scanning tunneling microscopy to obtain layer-by-layer cross sections of deposits on substrate.[55] In other studies, it was found that layer-by-layer growth of the first two layers of Pd on Au(111) was followed by up to ten levels of quasi-layer-by-layer island growth.[7] Experimental heteroepitaxial deposition systems of interest include silver onto crystalline and amorphous substrates (silicon and glassy carbon),[61] and palladium deposition on Au(111).[7] The effect of additives, potential control and varying bulk gold concentrations has been studied for a system of gold deposition onto n-Si(100).[62]

For our numerical investigation, the simulation surface was a 2-D domain with 256 by 256 lattice sites with a 'single-atom' seed nucleus placed at the center. Incoming atoms were allowed to deposit on the Substrate and move about (according to the value D_S/F_S), and also on the newly-deposited Metal (according to the value of D_M/F_M). Atoms deposited on the metal layer were allowed to hop down to a lower layer $(\gamma = 1)$. Each calculation was run until a half-monolayer $(\theta = 0.5)$ was deposited; identical simulations were repeated one hundred times in order to obtain an average value for the nearest-neighbor distribution.

Figure 3 shows results for various combinations of D_S/F_S and D_M/F_M. Lines are drawn through the locus of points associated with a given average value of the average nearest-neighbor distance (five values between 7 and 25). The solid lines were computed by varying D values while keeping F constant, and the dashed lines by varying F values while keeping D constant. For the range of parameters shown in Figure 3, it may be seen that mostly the lines are horizontal, which indicates that the nearest-neighbor distribution is influenced primarily by the initial substrate ratios, D_S/F_S. The question is, will D_M/F_M ever play a role in determining the nucleation density? The simulations suggest that this can only happen when the flux onto the deposited layers is much higher than onto the substrate, the diffusion rates on both surfaces are the same, and there is a fast rate of diffusion over the edges (this last point is not shown, but the difference between the dashed and solid lines depends on the Erhlich-Swoebel barrier, and, as γ is lowered, all nucleation densities are a function of D_S/F_S).

Downloaded on 2014-06-20 to IP 128.111.41.122 address. Redistribution subject to ECS terms of use (see ecsdl.org/site/terms_use) unless CC License in place (see abstract).

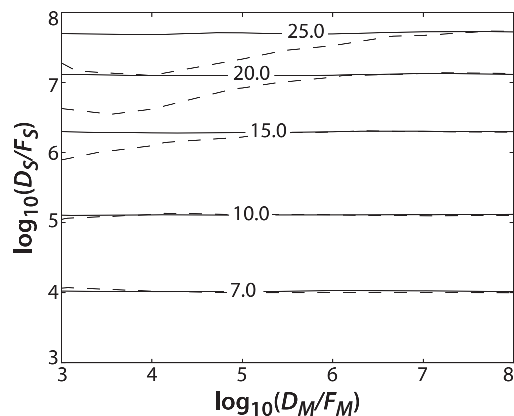

Figure 3. Contour lines of constant average nearest-neighbor distance for various D_S/F_S on the substrate, and D_M/F_M on deposited metal. The data was generated with $\gamma = 1$ (no ES barrier) and $\beta = 0.01$. For the solid lines, F is held constant and D is varied. For the dotted lines, D is held constant and F is varied.

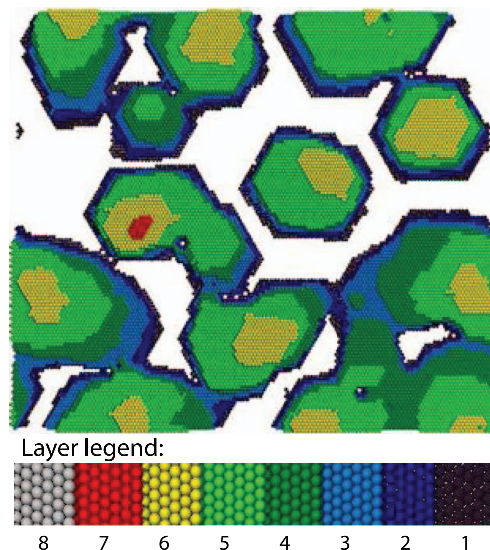

Figure 4. Three monolayer equivalent deposition under heteroepitaxial condition ($D_S/F_S = 10^7$, $D_M/F_M = 10^6$, $\beta = 0.01$, $\gamma = 0.1$). Values of γ closer to one lead to flatter and wider island profiles, while values of γ closer to zero lead to steeper and narrower island profiles.

A speedup of 5× for ELFPT over KMC was found for the cases with $F_S/F_M = 100$. This can be attributed to the smaller number of wider islands grown at these conditions, compared to a larger number of much smaller islands grown at a 1.5× speedup in the cases of $F_S/F_M = 0.01$. Again, the performance gain was more substantial for larger values of (D/F) and γ, and lower values of β.

Multilayer growth.— Multilayer deposition was investigated in homoepitaxial as well as heteroexpitaxial systems with the goal of examining the range of parameters between which systems exhibit either layer-by-layer growth or multi-nuclei growth. Adatoms arriving at an edge were allowed to move along the edge with a diffusion coefficient determined by Equation (1). Adatoms on a given layer were allowed to hop down to a lower layer to an extent determined by the Ehrlich-Schwöble barrier parameter γ, defined in Equation (2). The simulation surface was a 2-D domain with 128 by 128 lattice sites and a single atom seed nucleus in the center. Three monolayers ($\theta = 3$) were deposited in each simulation case, and each simulation was repeated ten times to obtain averages.

Figure 4 shows one instance of a surface found for $\theta = 3$ equivalent monolayers for the case of heteroepitaxial deposition ($D_S/F_S = 10^7$, $D_M/F_M = 10^6$, $\beta = 0.01$, $\gamma = 0.1$). It may be seen that multiple layers of islands nucleated and grew atop each other. For these conditions, new island layers nucleated and grew on top of successive layers before the lower layers grew laterally to match the footprint of the lowest layer. When γ was set to the limiting case of zero (infinite ES barrier, hop-down events not permitted), it was found each layer tended to grow to the edge of the lower layer, forming rough deposits with steep side walls. For values of γ close to 1, hop-down events occur readily, leading to layer-by-layer growth in the case of high (D/F).

A time-dependent intensity parameter[63] was used to distinguish between layer-by-layer growth, island growth and quasi-layer-by-layer growth. Figure 5(a) illustrates the variation of intensity parameter with the number of deposited monolayers for several values of γ, for the case of homoepitaxial deposition. For $\gamma = 1$ (fast hop-down rate), the intensity parameter oscillates with relatively small decay with each successive monolayer, a characteristic signature[63] that corresponds to a largely layer-by-layer growth mode. For $\gamma = 0.1$ (moderate hop down rate) the successive oscillations depicted in Figure 5(a) are damped more strongly, indicating a transition toward rough growth. Finally, for $\gamma = 0.01$ (slow hop down rate) the successive oscillations are damped even more quickly, and the surface is even rougher. The final surfaces are shown in Figures 5(b) through 5(d).

In heteroepitaxial systems, for conditions where the attachment rate to the initial substrate is slower than that to the subsequently deposited layers ($F_M < F_S$), islands were found to grow with steeper sidewalls because the substrate is starved for walkers. Growth modes similar to that seen in Figure 4 are more common in this regime, whereby nuclei quickly cover some large percentage of the original substrate, but then begin growing upward layer-by-layer on that new surface, rather than the substrate.

Finally, when the attachment rate to the substrate is faster than to the subsequently deposited layers ($F_M > F_S$), the island sites are much more softly-sloped (because they can adopt much larger bases). The order parameter method[63] is easily applied in this case, and the results look very similar to those of Figure 5 with more gentle decays.

A speedup of 10× for ELFPT over KMC was found for the case of $(D/F) = 10^9$, $\beta = 0.01$ and $\gamma = 1$. In general, the performance was

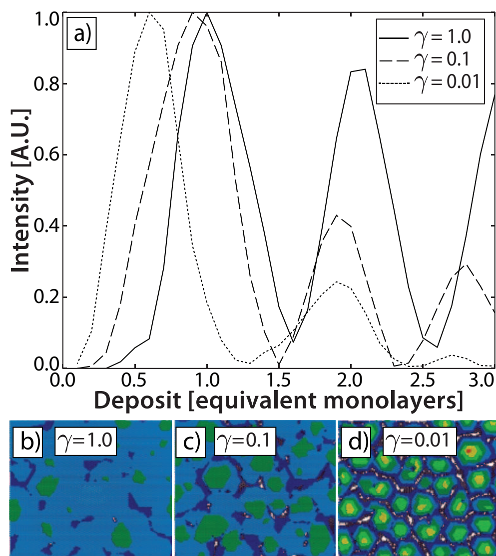

Figure 5. Dependence of the intensity parameter on the number of desired equivalent monolayers for homoepitaxial growth ($(D/F) = 10^6$, $\beta = 0.01$). The figure shows the effect of varying the Ehrlich-Schwöbel barrier parameter, γ, on the types of surface growth. Note: Color key is the same as in Figure 4.

Downloaded on 2014-06-20 to IP 128.111.41.122 address. Redistribution subject to ECS terms of use (see ecsdl.org/site/terms_use) unless CC License in place (see abstract).

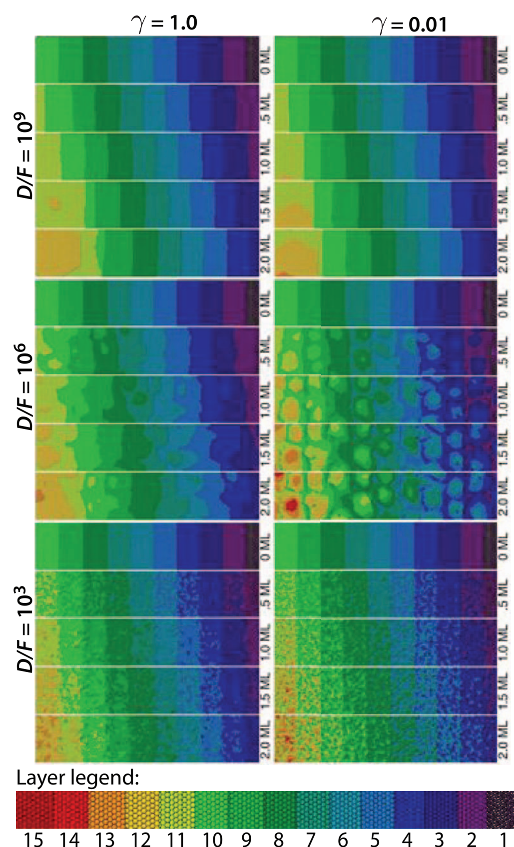

Figure 6. Multiple views of growth during homoepitaxial deposition on monoatomically high terraces of width 24 atoms with an edge diffusivity parameter β set to 0.01. The six panels correspond to different combinations of D/F and γ indicated in the margins. Each panel consists of 5 strips, which correspond (from top to bottom) to 0, 0.5, 1.0, 1.5, and 2.0 equivalent monolayers of deposit. The color bar shows the color coding for the different layers. Animated sequences of these simulations can be found in auxiliary materials online (see Supplementary Materials S1).

found to be enhanced for higher values of (D/F) and γ, and lower values of β.

Stepped terraces.— Terraces and step edges have been widely exploited for their propensity to form nuclei in the fabrication of nano-wires and nano-ribbons by "step edge decoration". Formation of nanowires at step edges has been reported using physical vapor deposition,[64] and using molecular beam epitaxy on a stepped Au/Si(111) substrate.[65] In electrochemical systems, deposition onto highly ordered pyrolytic graphite (HOPG) surfaces,[66,67] and onto Si(111) surfaces[68] led to formation of nanowires at the step edges. In addition, layer-by-layer growth and island formation on terraces[69] for Pd on Au systems as well as evidence for an Ehrlich-Schwöbel barrier at step edges at solid/liquid interfaces[11] of Au on Au have been observed.

The simulation surface consisted of a domain of 256 by 256 atoms with an initial configuration of atomically flat terraces of straight mono-atomic steps. Terrace widths between 16 and 40 atoms were investigated. Step edges represent sites to which adatoms can attach. Depending on the ES-barrier, adatoms on one level can hop down to a lower level. Results for the step width of 24 atomic units are presented in Figure 6. Boundaries at the uppermost and lowermost layers of the simulation domain were chosen to be reflective and inert. The boundaries perpendicular to the step edges were set to be periodic. The incoming flux rate was statistically uniform over the entire simulation domain. Simulations were carried out until a total of 2 equivalent monolayers were deposited.

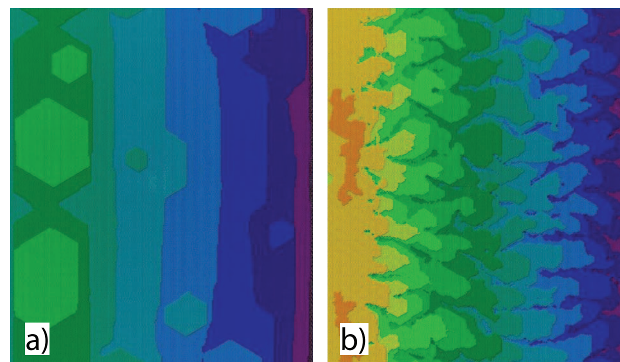

Figure 7. Growth on stepped terraces. a) $(D/F) = 10^9$, $\beta = 0.01$, $\gamma = 0.01$. Final surface morphology after deposit of 2 equivalent monolayers in stepped terraces of width 40. More nuclei appear on stepped terrace compared to the case with steps of width 24. b) $(D/F) = 10^6$, $\beta = 10^{-6}$, $\gamma = 1$. Very low edge diffusivity leads to more fractal shapes of islands. Note: Color key is the same as in Figure 6.

Figure 6 shows the results as a series of top-down views of simulated growth patterns on monoatomically high terraces. For each parameter set (step width, (D/F) and γ) there are 5 strips of roughly 50×256 atoms at different coverage levels. The top strip is at $\theta = 0$ and each subsequent strip has an additional coverage of 0.5 ML.

The upper left image in Figure 6 shows the case of fast diffusion/low deposition rate and no ES Barrier ($D/F = 10^9$; $\gamma = 1$). In this case each of the terraces moves to the right by lateral growth at the step edge. Such behavior is a result of the low adatom density on each terrace, which makes the formation of wild nuclei highly unlikely. For the 24-atom terraces shown here, rapid diffusion of adatoms results either in attachment to the upper step edges, or movement onto a lower terrace. In both cases, the result is lateral growth along the step edge with very little formation of wild nuclei. The presence of a high ES barrier (upper right panel; $(D/F) = 10^9$, $\gamma = 10^{-3}$) serves to block movement to lower terraces, causing the diffusion distance to the growth edge to double. For the parameters associated with the upper right panel, it was found (not shown here) that island formation on terraces was seen only for step-widths of 40 and above.

At medium influx of adatoms ($(D/F) = 10^6$) in the absence of an ES barrier ($\gamma = 1$), the central left image in Figure 6 illustrates that the original terraced surface develops by lateral growth at the step edges, in part owing to adatoms dropping down from upper terraces. In this case, however, a small number of wild nuclei grow on each of the terraces. However, the lateral movement of the step is faster than the upward growth of wild nuclei/islands into multilayer mounds. It may be seen that accretion of the islands into the advancing step edges causes them to become distorted. For the case of a high ES barrier (central right image, $\gamma = 10^{-2}$), adatoms arrive at step edges by diffusing on the same level, as opposed to dropping down from the next highest layer. As a result, adatoms are more likely to attach to nuclei growing on each terrace (rather than to disappear over the edge to the next layer), resulting in more pronounced upward growth of islands on the terraces.

The bottom left image in Figure 6 shows the case of high influx of adatoms and no ES Barrier ($(D/F) = 10^3$; $\gamma = 1$), for which it may be seen that many small islands nucleate at sites that are dispersed over the terraces. Mobile adatoms on a given terrace either attach to the edge of islands, resulting in their lateral growth, or drop over the step edge onto a lower terrace. The lower right image shows the effect of a high ES Barrier, which hinders the movement of adatoms over terrace edges onto lower surfaces. The result is a higher concentration of adatoms on a given terrace, with in more island nucleation as well as multiple layers of growth onto "off-shore" islands.

Figure 7 shows a set of examples grown under different conditions from those in Figure 6. The width of step edges can be varied to control the growth mode. Figure 7(a) shows the final topology for

Downloaded on 2014-06-20 to IP 128.111.41.122 address. Redistribution subject to ECS terms of use (see ecsdl.org/site/terms_use) unless CC License in place (see abstract).

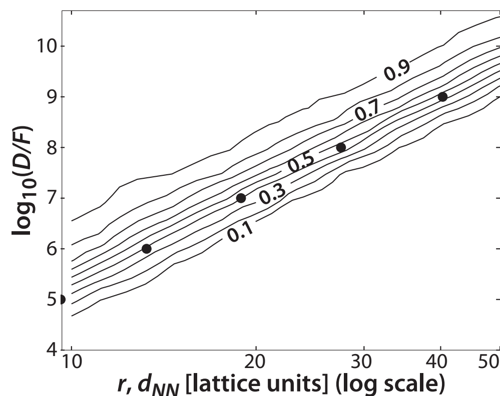

Figure 8. Probability to grow a single crystal in a hexagon of given radius and (D/F) ratio plotted in a log-log scale. The black markers correspond to the mean nearest-neighbor values computed for homoepitaxy on unconfined flat surfaces.

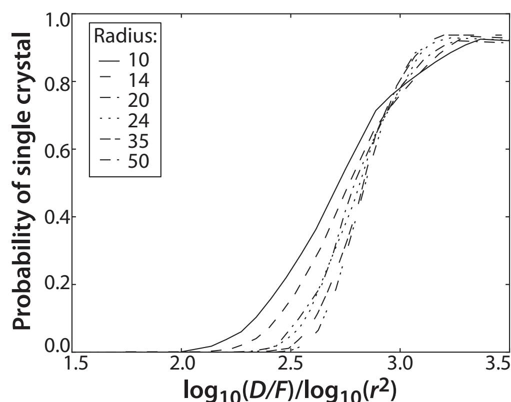

Figure 9. Single crystal probability as function of Λ for different radii of the confined areas. The value of Λ is a good estimator for the probability of single crystal growth. Values of $\Lambda < 2.5$ indicate negligible chance of single crystal growth and values of $\Lambda > 3.0$ indicate high probability of single crystal growth.

growth under the same conditions as the top right image in Figure 6, $(D/F) = 10^9$, but grown on steps of width 40 lattice units. As opposed to the growth on steps of width 24 lattice units, islands form on the terraces, due the larger surface available for nucleations. Figure 7(b) shows the effect of a reduced edge diffusivity of adatoms ($\beta = 10^{-6}$) on a domain with terraces of width 24 and $(D/F) = 10^6$. The low edge diffusivity results in rather fractal step edges. Interestingly, the mean distance between the fractal step edges appears to remain constant over the time of deposition of 2 equivalent monolayers.

For stepped growth, a speedup of 10× over KMC or more is possible with ELFPT if the Ehrlich-Schwöbel barrier is kept low (high γ). Small terrace widths limit the maximum possible size of the protection zone, which lowers the performance gain. The best performance of ELFPT over KMC is reached for high values of (D/F) and γ, and low values of β. Both methods suffer serious absolute performance losses when edge diffusivity is high ($\beta > 1.0$), and the ES barrier is high ($\gamma > 0.1$).

Single crystal probability in confined area.— The fabrication by electrodeposition of nanodot arrays of magnetic alloys for use in next-generation ultra-high-density recording media has been reported with the use of nano-templates that confine the deposition area.[70,71] The quality of these devices depends heavily on the ability to deposit single crystals with well-defined orientation in order to optimize coercivity properties.[11,72–74] Single crystal growth in small confined areas has also been reported for germanium electrodeposition onto Si surfaces.[75]

These examples raise the question of under what range of operating conditions is it possible to anticipate electrodeposition of a single crystal in a confined region. We address this question by computing the probability that a single nucleus formed on the confined area of an atomically-flat substrate will grow laterally to cover the entire region before another nucleus would form on that layer. If each layer grows epitaxially in a like manner, then the result would be a single crystal.

To address this question, simulations were carried out for homoepitaxial deposition onto an atomically-smooth defect-free lattice confined within inert reflecting walls. For the HCP(0002) lattice, the deposition surface was chosen to be a hexagon of given radius R in lattice parameters, which corresponded approximately to the circular cross section of nano-pipettes investigated experimentally.[73] Adatoms were assumed to be free to diffuse within the confined area. A 'single crystal' was defined as an island that grew from a single nucleation site to cover the entire domain of each layer of deposit. Simulations were carried out until two equivalent monolayers were deposited. Ten values of (D/F) in the range 10^4 to 10^{10}, and ten values of R in the range of 10–50 lattice units were investigated, with $\beta = 1$ and $\gamma = 1$. For each of the 100 combinations of (D/F) and R, 1000 runs were carried out to determine empirically the probability of obtaining a single crystal deposit.

Over the range of parameters investigated, Figure 8 shows probability contours between 0.1 and 0.9. Contours were generated by simulating 1000 runs at 100 points in parameter space. The 95% confidence intervals for the probabilities are less than ± 0.03 at any given point. It may be seen that the probability-contours follow a power-law when plotted in a $\log_{10} D/F$ vs. $\log_{10} R$ plot. For example, doubling the radius of the confined area requires a factor of nearly 100× increase in (D/F) to maintain the same probability of growing single crystals. For a given value of R, the results in Figure 8 indicate that an increase in probability from 0.5 to 0.95 would require an increase in (D/F) of two orders of magnitude.

The probability of growing a single crystal appears to follow the same power law as the mean nearest-neighbor distance d_{NN} (Figure 2). This means that if the diameter of the confined area is chosen to be significantly smaller (i.e. 50% smaller) than the d_{NN} value for a given (D/F) on an unconstrained surface, the probability to grow single crystals is high (> 90%). Conversely, if the diameter of the confined hexagon is chosen to be equal to or larger than d_{NN}, then the probability to grow single crystals is 50% or less.

The linear correlation in the log-log plot of Figure 8 suggests that scaling of $\log_{10}(D/F)$ with the log of the square of the radius of the confined area may provide an empirical estimator for the probability of single crystal growth. We have plotted the results in Figure 9, where we define Λ as

$$\Lambda = \frac{log_{10}(D/F)}{log_{10}(r^2)}. \quad [4]$$

If the value of Λ is greater than 3.0, the probability to grow single crystals is greater than 80%, and if the value of Λ is below 2.0, the probability to grow single crystals is essentially non-existent. While these results provide a first step toward identifying feasible conditions, they give neither necessary nor sufficient conditions since no account is taken of lattice-mismatch, non-epitaxial behavior, or post-deposition ripening phenomena. For that reason, they may be regarded as advisory for experimentalists seeking to reduce intuition to practice.

A speedup of 8× for ELFPT over KMC was observed for the case of $(D/F) = 10^9$, $\beta = 0.01$ and $\gamma = 1$ and a radius of 85. As for most cases, the performance gain is more substantial for high values of (D/F) and γ, and low values of β. Larger radii allow for larger protection zones, so ELFPT is generally favored for larger confined areas.

Conclusions

A stochastic atomic-scale lattice-based numerical algorithm was developed for simulating of early stages of kinetically controlled

Downloaded on 2014-06-20 to IP 128.111.41.122 address. Redistribution subject to ECS terms of use (see ecsdl.org/site/terms_use) unless CC License in place (see abstract).

electrochemical nucleation and growth processes. Numerical computations were carried out with a model system that included the flux of atoms arriving at an hcp(0002) surface lattice, 2-D surface diffusion of adatoms, 1-D edge diffusion along step edges, and movement across step edges according to an Ehrlich-Schwöbel barrier. The computational method, based on the First Passage Time approach, was found to be particularly advantageous over kinetic Monte Carlo for high values of (D/F), under which conditions the concentration of adatoms is so low that individual adatoms diffuse over large distances before encountering one another (nucleating) or attaching to an island edge. The performance gain makes possible atomic-scale resolution while also exploring previously too-costly parameter regimes (high (D/F)) on sufficiently large-areas needed to obtain statistical characterization of deposit morphology for comparison with experimental data.

Five categories of deposition systems were investigated: homoexpitaxy, heteroepitaxy, multi-layer, step edge, and confined regions. Homoepitaxial growth was used to verify that the average nearest-neighbor-distance between nuclei is a function of (D/F) (Figure 1), and that the probability of finding a neighbor nucleus scaled as $rN^{1/2}$ (Figure 2) in agreement with literature benchmarks. In heteroepitaxial systems, the nearest-neighbor distribution was found to be primarily influenced by the value of D_S/F_S on the substrate (Figure 3). The smooth/rough character of heteroepitaxial multilayer growth was found to be sensitive to the relative magnitude of F_S and F_M as well as to the Ehrlich-Schwöbel barrier (Figure 4).

Analysis of multilayer growth morphology simulations with a time-dependent intensity parameter was used to distinguish between layer-by-layer growth, island growth, and quasi-layer-by-layer growth (Figure 5). Nucleation on stepped terraces was found only when the width of the terrace is large compared to the exclusion zone adjacent to the step edges. That is, large values of (D/F) and a low Ehrlich-Schwöbel barrier favors layer-by-layer growth at step edges, while a high Ehrlich-Schwöbel barrier contributes to nucleation and vertical multilayer growth of islands on the terraces (Figure 6). Regions under which a low edge diffusivity can result in a rough step edge profile were identified (Figure 7).

The probability of growing single crystals in a small confined region is strongly dependent on the area of confinement and the value of (D/F) (Figure 8). For a hexagon area of radius r, it was found that the parameter $\log_{10}(D/F)/\log_{10}(r^2))$ collapses the transition region between single nucleus and multiple nuclei into a relatively narrow band (Figure 9).

The simulation approach presented in this work has the potential to contribute well beyond the pristine examples described here for its initial development. The value of experimental data from well-characterized systems in guiding such extensions should not be underestimated. Depending on the experimental arrangement, the additional phenomena that could be incorporated in the physical model used here for simulations could include potential dependence of the incoming flux, additional surface species associated with additives, additional deposition fluxes associated with alloys, and reversible dissolution of nuclei and islands, to name a few. In addition, it may be worthwhile to take advantage of high-speed stochastic algorithms to run larger numbers of computational runs in order to fit computed results to experimental data, and thus enable parameter estimation and optimization. Such extensions offer the promise for improved molecular engineering development procedures for the rational design of next-generation devices.

Acknowledgments

This research was supported through grant DE-FG02-12ER26085 from the U.S. Department of Energy. We acknowledge support from the Center for Scientific Computing from the California NanoSystems Institute, the Materials Research Lab (NSF MRSEC DMR-1121053), and NSF CNS-0960316. Andri Bezzola and Benjamin B. Bales contributed equally to this work

List of Symbols

β	Edge diffusion parameter [-], defined in Equation (1)
χ	Nucleation density scaling exponent [-], defined in Equation (3)
γ	ES parameter [-], defined in Equation (2)
Λ	Single crystal probability parameter [-], defined in Equation (4)
θ	Coverage / amount of deposited metal [ML]
D	Surface diffusivity coefficient [(lattice units)$^2 s^{-1}$]
D_M	Diffusivity of adatom on deposited metal [(latticeunits)$^2 s^{-1}$]
D_S	Diffusivity of adatom on substrate material [(latticeunits)$^2 s^{-1}$]
D_{edge}	Edge Diffusivity [(lattice units)$^2 s^{-1}$], defined in Equation (1)
D_{ES}	Diffusivity over ES barrier (step edge) [(lattice units)$^2 s^{-1}$], defined in Equation (2)
F	Flux density of adatoms to the surface [(lattice units)$^{-2} s^{-1}$]
F_M	Flux density of adatoms to deposited metal [(latticeunits)$^{-2} s^{-1}$]
F_S	Flux density of adatoms to the substrate [(latticeunits)$^{-2} s^{-1}$]
N	Nucleation density [(site)$^{-1}$], defined in Equation (3)
$P(r)$	Probability to find at least one neighbor within distance r from COM of any given island [-]
COM	Center of mass
ML	Equivalent monolayers

References

1. H. Brune, *Surf. Sci. Rep.*, **31**(3-4), 125 (1998).
2. E. Dobisz, Z. Bandic, and T. Albrecht, *Proc. IEEE*, **96**(11), 1836 (2008).
3. I. Gonzalez-Valls and M. Lira-Cantu, *Energy Environ. Sci.*, **2**(1), 19 (2009).
4. I. Paramasivam, H. Jha, N. Liu, and P. Schmuki, *Small*, **8**(20), 3073 (2012).
5. R. Deshpande, M. Verbrugge, Y.-T. Cheng, J. Wang, and P. Liu, *J. Electrochem. Soc.*, **159**(10), A1730 (2012).
6. M. Mavrikakis, B. Hammer, and J. Nørskov, *Phys. Rev. Lett.*, **81**(13), 2819 (1998).
7. L. Kibler, M. Kleinert, R. Randler, and D. Kolb, *Surf. Sci.*, **443**, 19 (1999).
8. L. A. Kibler, Preparation and Characterization of Noble Metal Single Crystal Electrode Surfaces. Technical report, International Society of Electrochemistry (2003).
9. P. Allongue and F. Maroun, *J. Phys. Cond. Mater.*, **18**(10), S97 (2006).
10. S. a. Policastro, J. C. Carnahan, G. Zangari, H. Bart-Smith, E. Seker, M. R. Begley, M. L. Reed, P. F. Reynolds, and R. G. Kelly, *J. Electrochem. Soc.*, **157**(10), C328 (2010).
11. T. Ouchi, Y. Arikawa, T. Kuno, J. Mizuno, S. Shoji, and T. Homma, *IEEE Trans. Magn.*, **46**(6), 2224 (2010).
12. Q. Huang, K. Reuter, S. Amhed, L. Deligianni, L. T. Romankiw, S. Jaime, P.-P. Grand, and V. Charrier, *J. Electrochem. Soc.*, **158**(2), D57 (2011).
13. E. Budevski, G. Staikov, and W. Lorenz, In *Electrochem. Phase Form. Growth*. VCH, Weinheim, Germany (1996).
14. K. J. Vetter, *Electrochemical Kinetics : theoretical and experimental aspects*. Academic Press, New York (1967).
15. A. Milchev, *Electrocrystallization*. Kluwer Academic Publishers, Boston (2002).
16. R. D. Braatz, D. Kolb, J. Lipkowski, and P. N. Ross, In R. C. Alkire, D. M. Kolb, J. Lipkowski, and P. N. Ross, editors, *Electrochem. Surf. Modif.*, Advances in Electrochemical Sciences and Engineering, chapter 4. Wiley-VCH Verlag GmbH & Co. KGaA, Weinheim, Germany (2008).
17. A. Bezzola, B. B. Bales, R. C. Alkire, and L. R. Petzold, *J. Comput. Phys.*, **256**, 183 (2014).
18. E. G. Seebauer and C. E. Allen, *Prog. Surf. Sci.*, **49**(3), 265 (1995).
19. E. G. E. Seebauer and M. Y. L. M. Jung, *Springer*, **42A1**, 455 (2001).
20. A. B. Bortz, M. H. Kalos, and J. L. Lebowitz, *J. Comput. Phys.*, **17**(1), 10 (1975).
21. M. Schroeder, P. Smilauer, and D. E. Wolf, *Phys. Rev. B*, **55**(16), 10814 (1997).
22. S. J. Liu, H. Huang, and C. H. Woo, *Appl. Phys. Lett.*, **80**(18), 3295 (2002).
23. C. Ratsch and J. A. Venables, *J. Vac. Sci. Technol. A Vacuum, Surfaces, Film.*, **21**(5), S96 (2003).
24. R. M. Stephens and R. C. Alkire, *J. Electrochem. Soc.*, **154**(8), D418 (2007).
25. C. Ratsch, A. Zangwill, P. Šmilauer, and D. Vvedensky, *Phys. Rev. Lett.*, **72**(20), 3194 (1994).
26. A. Chatterjee and D. G. Vlachos, *J. Comput. Mater. Des.*, **14**(2), 253 (2007).
27. L. Mandreoli, J. Neugebauer, R. Kunert, and E. Schöll, *Phys. Rev. B*, **68**(15), 155429 (2003).
28. G. Russo, L. Sander, and P. Smereka, *Phys. Rev. B*, **69**(12), 121406 (2004).
29. J. DeVita, L. Sander, and P. Smereka, *Phys. Rev. B*, **72**(20), 205421 (2005).
30. M. Gyure, C. Ratsch, B. Merriman, R. Caflisch, S. Osher, J. Zinck, and D. Vvedensky, *Phys. Rev. E*, **58**(6), R6927 (1998).
31. R. Caflisch, M. Gyure, B. Merriman, S. Osher, C. Ratsch, D. Vvedensky, and J. Zinck, *Appl. Math. Lett.*, **12**(4), 13 (1999).

Downloaded on 2014-06-20 to IP 128.111.41.122 address. Redistribution subject to ECS terms of use (see ecsdl.org/site/terms_use) unless CC License in place (see abstract).

32. S. Chen, B. Merriman, M. Kang, R. E. Caflisch, C. Ratsch, L.-T. Cheng, M. Gyure, R. P. Fedkiw, C. Anderson, and S. Osher, *J. Comput. Phys.*, **167**(2), 475 (2001).
33. T. O. Drews, E. G. Webb, D. L. Ma, J. Alameda, R. D. Braatz, and R. C. Alkire, *AIChE J.*, **50**(1), 226 (2004).
34. E. Rusli, F. Xue, T. O. Drews, P. M. Vereecken, P. Andricacos, H. Deligianni, R. D. Braatz, and R. C. Alkire, *J. Electrochem. Soc.*, **154**(11), D584 (2007).
35. J. Liu, C. Liu, and P. P. Conway, *Electrochim. Acta*, **54**(27), 6941 (2009).
36. R. M. Stephens and R. C. Alkire, *J. Electrochem. Soc.*, **156**(1), D28 (2009).
37. C.-C. Chou and M. L. Falk, *J. Comput. Phys.*, **217**(2), 519 (2006).
38. M. Bartelt and J. Evans, *Phys. Rev. B*, **46**(19), 12675 (1992).
39. M. C. Bartelt and J. W. Evans, *Phys. Rev. B*, **54**(24), R17359 (1996).
40. X. Xia, S. Xie, M. Liu, H.-C. Peng, N. Lu, J. Wang, M. J. Kim, and Y. Xia, *Proc. Natl. Acad. Sci. U. S. A.*, **110**(17), 6669 (2013).
41. L. Guo, S. Zhang, and P. Searson, *Phys. Rev. E*, **79**(5), 051601 (2009).
42. L. Guo and P. C. Searson, *Electrochim. Acta*, **55**(13), 4086 (2010).
43. L. Guo, G. Oskam, A. Radisic, P. M. Hoffmann, and P. C. Searson, *J. Phys. D. Appl. Phys.*, **44**(44), 443001 (2011).
44. J. Krug, P. Politi, and T. Michely, *Phys. Rev. B*, **61**(20), 14037 (2000).
45. S. Redner, *A Guide To First-Passage Processes*. Cambridge University Press, Cambridge (2001).
46. T. Opplestrup, V. Bulatov, G. Gilmer, M. Kalos, and B. Sadigh, *Phys. Rev. Lett.*, **97**(23), 230602 (2006).
47. V. I. Tokar and H. Dreyssé, *Phys. Rev. E*, **77**(6), 066705 (2008).
48. T. Oppelstrup, V. V. Bulatov, A. Donev, M. H. Kalos, G. H. Gilmer, and B. Sadigh, *Phys. Rev. E*, **80**(6), 066701 (2009).
49. R. Ramaswamy and I. F. Sbalzarini, *J. Chem. Phys.*, **135**(24), 244103 (2011).
50. T. Jahnke and D. Altntan, *BIT Numer. Math.*, **50**(4), 797 (2010).
51. G. Nandipati, Y. Shim, and J. G. Amar, *Phys. Rev. B*, **81**(23), 235415 (2010).
52. H.-J. Ernst, F. Fabre, R. Folkerts, and J. Lapujoulade, *Phys. Rev. Lett.*, **72**(1), 112 (1994).
53. Y. Shim and J. Amar, *Phys. Rev. B*, **73**(3), 035423 (2006).
54. Y. He and E. Borguet, *Faraday Discuss.*, **121**, 17 (2002).
55. H. Naohara, S. Ye, and K. Uosaki, *J. Electroanal. Chem.*, **473**(1-2), 2 (1999).
56. K. Krug, J. Stettner, and O. Magnussen, *Phys. Rev. Lett.*, **96**(24), 246101 (2006).
57. O. Magnussen, K. Krug, a.H. Ayyad, and J. Stettner, *Electrochim. Acta*, **53**(9), 3449 (2008).
58. F. Golks, J. Stettner, Y. Gründer, K. Krug, J. Zegenhagen, and O. M. Magnussen, *Phys. Rev. Lett.*, **108**(25), 256101 (2012).
59. C. Vaz-Domínguez and A. Cuesta, *Electrochim. Acta*, **56**(19), 6847 (2011).
60. A. Ayyad, J. Stettner, and O. Magnussen, *Phys. Rev. Lett.*, **94**(6), 066106 (2005).
61. K. Marquez, G. Staikov, and J. Schultze, *Electrochim. Acta*, **48**, 875 (2003).
62. Q. Huang, H. Deligianni, and L. T. Romankiw, *J. Electrochem. Soc.*, **153**(5), C332 (2006).
63. T. Huhtamäki, M. Jahma, and I. Koponen, *Nucl. Instruments Methods Phys. Res. Sect. B Beam Interact. with Mater. Atoms*, **264**(1), 55 (2007).
64. F. J. Himpsel, T. Jung, and J. E. Ortega, *Surf. Rev. Lett.*, **04**(02), 371 (1997).
65. J. L. Liu, S. J. Cai, G. L. Jin, and K. L. Wang, *Electrochem. Solid-State Lett.*, **1**(4), 188 (1998).
66. E. C. Walter, B. J. Murray, F. Favier, G. Kaltenpoth, M. Grunze, and R. M. Penner, *J. Phys. Chem. B*, **106**(44), 11407 (2002).
67. R. M. Penner, *J. Phys. Chem. B*, **106**(13), 3339 (2002).
68. K.-i. Hara and I. Ohdomari, *Jpn. J. Appl. Phys.*, **37**(Part 2, No. 11A), L1333 (1998).
69. H. Naohara, S. Ye, and K. Uosaki, *J. Phys. Chem. B* (1998).
70. I. U. Schuchert, M. E. T. Molares, D. Dobrev, J. Vetter, R. Neumann, and M. Martin, *J. Electrochem. Soc.*, **150**(4), C189 (2003).
71. D. Dobrev, J. Vetter, N. Angert, and R. Neumann, *Appl. Phys. A Mater. Sci. Process.*, **69**(2), 233 (1999).
72. Y. Kamata, A. Kikitsu, H. Hieda, M. Sakurai, K. Naito, J. Bai, and S. Ishio, *Jpn. J. Appl. Phys.*, **46**(3A), 999 (2007).
73. T. Ouchi, Y. Arikawa, and T. Homma, *J. Magn. Magn. Mater.*, **320**(22), 3104 (2008).
74. T. Ouchi, Y. Arikawa, Y. Konishi, and T. Homma, *Electrochim. Acta*, **55**(27), 8081 (2010).
75. Q. Huang, S. W. Bedell, K. L. Saenger, M. Copel, H. Deligianni, and L. T. Romankiw, *Electrochem. Solid-State Lett.*, **10**(11), D124 (2007).

Downloaded on 2014-06-20 to IP **128.111.41.122** address. Redistribution subject to ECS terms of use (see **ecsdl.org/site/terms_use**) unless CC License in place (see abstract).